Simulation of Tig Weld on a ST355 plat

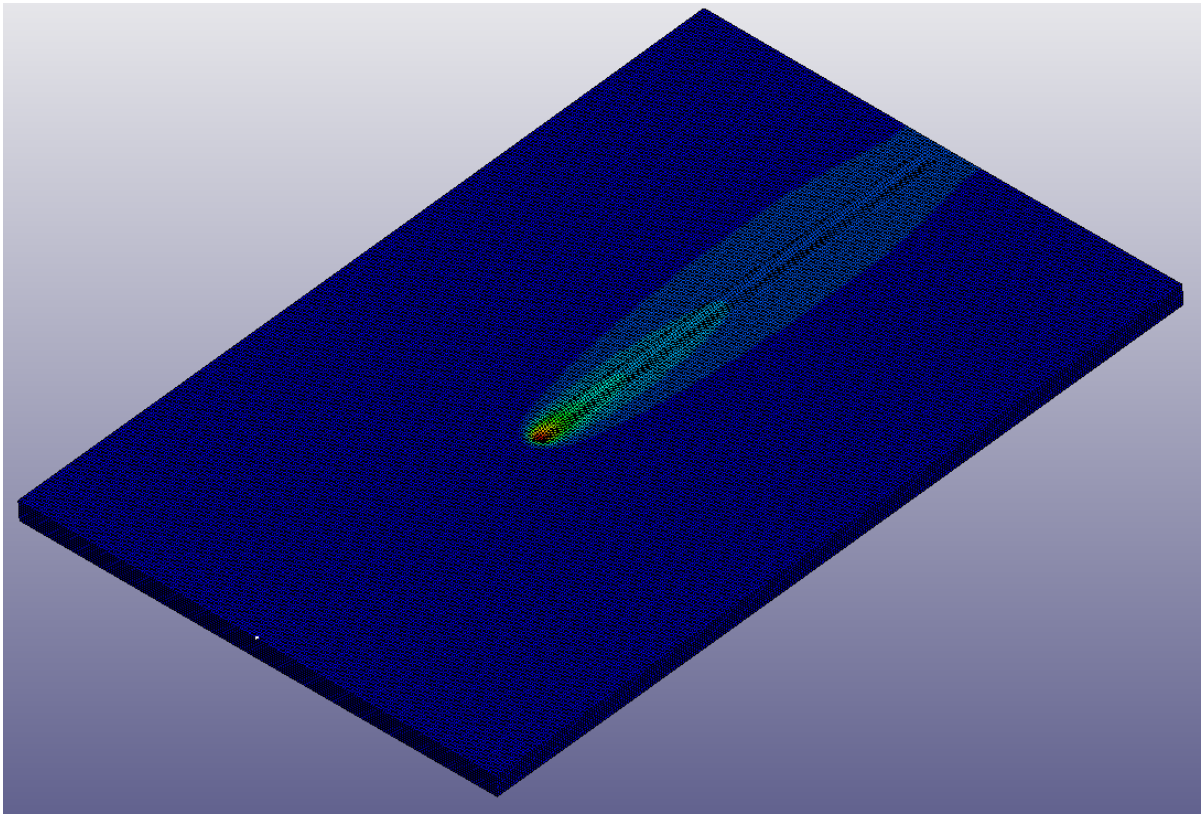

Master's Thesis

Jesper Pilgaard Koldsø
Material Technology
Aalborg University

20th August 2012

AALBORG UNIVERSITY
STUDENT REPORT

Master's Thesis at the Department of Materials and Production
Master in Materials Technology
Fibigerstræde 16
9220 Aalborg Øst
http://www.ses.aau.dk

Title:

Simulation of a Tig-Weld on a ST355 steel plate

Project:

Master's Thesis

Project duration:

8th April 2020 - 20th August 2020

Participant:

Jesper Pilgaard Koldsø

Supervisors:

Benny Endelt
Mikael Larsen

Abstract:

In this project, the simulation done in the paper: "Solid-state phase transformation and strain hardening on the residual stresses in S355 steel weldments" [Sun et al., 2019] will be recreated, and - if possible - improved. This is done by using LS-Dyna's material model `MAT_UHS_STEEL`, and since the efficiency was not given in the paper, it had to be found by trial and error. The efficiency was found to be 50% which is quite low according to the sources Jeberg [2005]; Karkhin [2013].
There were some differences between the data and the simulation done in [Sun et al., 2019], which was fist attributed to a wrong convection boundary condition. This was tested by lowering the convection constant to a fourth, but since this did not produce a significant change, this could not be the reason. Thereafter, it was found that if the efficiency was raised to 75%, there simulation fit the data well, and it could be used to predict the grain structure with a accuracy of 5%, where Sun et al. [2019] had an accuracy of 9%.
Therefore it was concluded that this was an improvement of the original model.

Number of pages: 42
Appendices: 2
Ended: 20-08-2020

Preface

This project is a master Thesis made by a Jesper Pilgaard Koldsø from the master-programme Materials Technology at Aalborg University. The goal of this project is is to recreate and possible improve the simulation don in the paper titled "Solid-state phase transformation and strain hardening on the residual stresses in S355 steel weldments" [Sun et al., 2019]. This was don using LS-dyna with the material model `MAT_UHS_STEEL`.

Readers guide

The reference method used throughout this report is the Harvard-method. This means that the references will be mentioned as [Last name, Year], with the remaining information about the reference to be found in the bibliography. The books in the bibliography are listed as: Title, author(s), year of release, ISBN, along with the publisher and edition. Internet sites will be listed as: Author(s), title, URL, release year and the day it was visited.

This thesis contains a summary of the contents of this thesis in danish since it is a demand.

Resumé (in Danish)

I dette projekt er det forsøgt at genskabe resultaterne fra svejsesimuleringen, som er blevet præsenteret i artiklen: "Solid-state phase transformation and strain hardening on the residual stresses in S355 steel weldments".

I denne artikel er setuppet en ST-355 stålplade med dimensionerne 300 mm × 200 mm × 8 mm, hvor der bliver lavet en TIG-svejsning op langs midten af pladen. Dette er blevet gjort med indstillingerne, som kan ses i tabellen 2.1. Derefter blev der lavet en simulering, som er blevet sammenlignet med resultaterne fra svejsningen. Der er dog en forskel på resultaterne, eftersom køletiden fra 800 °C til 500 °C for den simulerede svejsning er 13,2 s, hvor den for den målte svejsningen var 21,6 s. Disse forskelle var også til stede ved udregningen af kornstrukturen, hvor simuleringen forudsagde, at der ville være 42% ferrit og pearlit og 58% bainit. Det blev dog målt til at være 51% ferrit og pearlit og 49% bainit for den aktuelle svejsning.

Den første opgave var at genskabe resultaterne fra simuleringen i artiklen. Dette er blevet gjort ved hjælp af programmet LS-Dyna med materialemodellen `MAT_USH_STEEL`. Denne model har en implementering af Kirkaldys model, som er en fænomenologisk model til at forudsige kornstrurkturen. Denne simulering er blevet opsat og gav en køletid på 11,3 s, som er ganske tæt på artiklens 13,2 s. Kornstrukturen, som den har forudsagt, er på 26% ferrit og pearlit, 68% bainit og 6% martensit. Dette er dog en støre afvigelse end resultatet fra artiklen. Simuleringen passer ca. ligeså dårligt som artiklens, og derfor er der blevet der set på adskillige forbedringsmuligheder. Først er det blevet forsøgt at sænke energitabet til omgivelserne, hvilket resulterede i en svag forbedring i køletiden til 12,1 s. Forudsigelsen på kornstrukturen er væsentligt bedre med 54% ferrit og pearlit, 45% bainit og 1% martensit, som er meget tæt på det målte. Køletiden er dog stadig meget lav i forhold til det målte, så derfor er forbedringen ikke væsentlig nok.

Derefter er energieffektiviteten blevet forøget fra 50% til 75%, hvilket resulterede i, at køletiden er steget til 23,7 s, hvilket er væsentligt tættere på 21,6 s, som det blev målt i artiklen. Kornstrukturen var dog noget helt andet, da den forudsagde 97% ferrit og pearlit, 2% bainit og 1% martensit. Dette var meget langt fra de målte værdiger, så derfor er Gibbs energien blevet justeret for disse formationsprocesser. Dette endte ud med at give et rimeligt resultat. Resultatet er blevet en forudsigelse på 56% ferrit og pearlit og 44% bainit, som synes meget tæt på det målte resultat.

Det kunne derfor konkluderes, at det var muligt både at genskabe resultatet fra artiklen og dertil lave nogle væsentlige forbedringer på simuleringen.

Contents

1 | Introduction

Welding is a common assembly method for metals that are very cheap Kalpakjian et al. [2014], but one of the problems with this method is that it leaves some residual stresses that can have a large effect on the fatigue properties of the assemble [Fuchs and Stephens, 1980].

These residual stresses are difficult to asses since several phenomena affect the stress state of a weld [Karkhin, 2013]. These stresses are mainly caused by the strains from thermal expansion/contraction as well as the volume change caused by the phases that are changing in the steel. The thermal strains can account for some of the stresses since the steel in front of the weld pool is expanding and the steel behind the weld pool is contracting. This will result in some large tensile stresses in the weld.

This effect is further complicated by the phase change, since steel undergoes a phase change from a body centre cubic(bcc) lattice called ferrite to a smaller face centre cubic(fcc) called austenite [Eisenhüttenleute, 1992]. This effect will negate some of the aforementioned thermal strains. However, in a steel, the carbon and iron will form cementite Fe_3C, and there will be certain differences in the properties of the weld depending on the arrangement of the ferrite and cementite[Eisenhüttenleute, 1992]. This leads to the formation of the phases pearlite, which consists of alternating layers of ferrite and cementite, and bainite where the ferrite is forming needle shapes with the cementite around the ferrite. Lastly, there is a phase called martensite which is formed when the cooling is so rapid that no other formation can be achieved. In this phase, the fcc lattice will distort to a bcc lattice that will introduce some shear stresses. The different phases all have different properties, where for example the martensite phase is a lot stronger then the ferrite pearlite phases. As a result, the residual stress will depend on the phase composition of the steel.

Because the phase composition of the weld has a high influence on the residual stresses in the weld, some attempts have been made over time to predict the phase composition of a steel weld. Such predictions are based on one of two models, the first being the JMAK model [Avrami, 1939], and the second being the Kirkaldy Model [Kirkaldy and Sharma, 1982].

One of the the more successful attempts is made in the paper Sun et al. [2019], where they made a welding simulation of an St355 steel plate, with the dimensions $200\,\text{mm} \times 300\,\text{mm} \times 8\,\text{mm}$. A mock-up of their setup can be seen in figure 1.1 and that figure is from the paper Sun et al. [2019]. The weld is a TIG-weld done without filament using the settings that can be found in table 1.1.

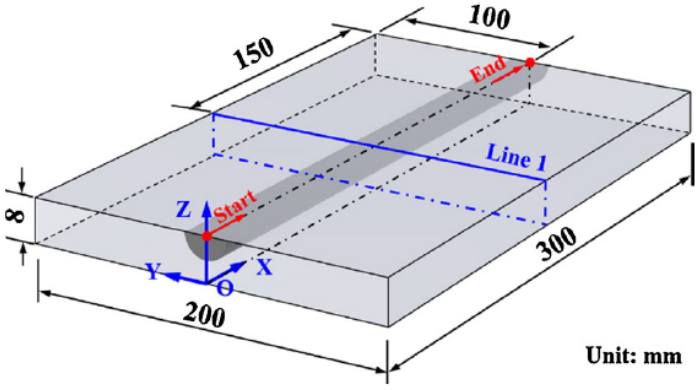

Figure 1.1: A mock-up of the setup don by Sun et al. [2019] and this figure is taken form Sun et al. [2019].

Current [A]	Voltage[V]	speed[$\frac{mm}{s}$]	Shielding gas
201	14.2	1.67	Ar

Table 1.1: Welding's input parameters

In this paper, a simulation of the weld is made to predict the hardness as a function of the weld. To do this the simulation attempts to predict the micro structure as a function of the weld.

The goal of the this project is to reproduce, and if possible improve, the simulation and the estimation of the grain structure results from the simulation done by Sun et al. [2019].

1.1 Theoretical Background to Phase Changes During Welding

Some phase change happens in steel when it is subjected to a welding process, and this has been common knowledge for some time [Eisenhüttenleute, 1992; Karkhin, 2013]. To understand which transformations are happening in the steel during the welding process, an iron-carbide phase-diagram is used. The important section of such a phase diagram can be seen on the right site of the figure 1.2 which has been obtained form the book Karkhin [2013]. Here there is a number of important pieces of information. Firstly, there is the vertical line that is named A_{c1}. This line is where pearlite(P) and austenite(γ) is in equilibrium. This means that if the temperature is over this line, pearlite will form to austenite, and if the temperature is below, austenite will form to pearlite. This temperature can be estimated by the the equation 1.1[Porter, 2018; Kоistinen and Marbürger, 1959; Oddy et al., 1996; Karkhin, 2013].

$$Ac_1 = 723 - 10.7Mn - 16.9Ni + 29Si + 16.9Cr + 290As + 6.4W \tag{1.1}$$

where the different elements shall be in wt%.

The next is the transformation temperature for the equilibrium of austenite and ferrite(α). This line is called A_{c3} and can be estimated as shown in equation 1.2. This equilibrium dos only exist if the carbon content is in the range of 0 % to 0.8 %

$$\begin{aligned} Ac_3 =& 912 - 203\sqrt{C} - 15.2Ni + 44.7Si + 104V + 31.5Mo + 13.1W - 30Mn - 11Cr + 20Cu \\ &+ 700P + 400Al + 120As + 400Ti \end{aligned} \tag{1.2}$$

This means that during heating, no changes well happen before the temperature is at A_{c1} where all the pearlite will start to from into austenite. At the same time, there will be an equilibrium between the content of ferrite and austenite until the temperature of A_{c3} is reached. Thereafter, all the ferrite starts to form into austenite Porter [2018]; Eisenhüttenleute [1992]. This is a major contributor to why there are so many zones in a weld, as can be seen in figure 1.2.

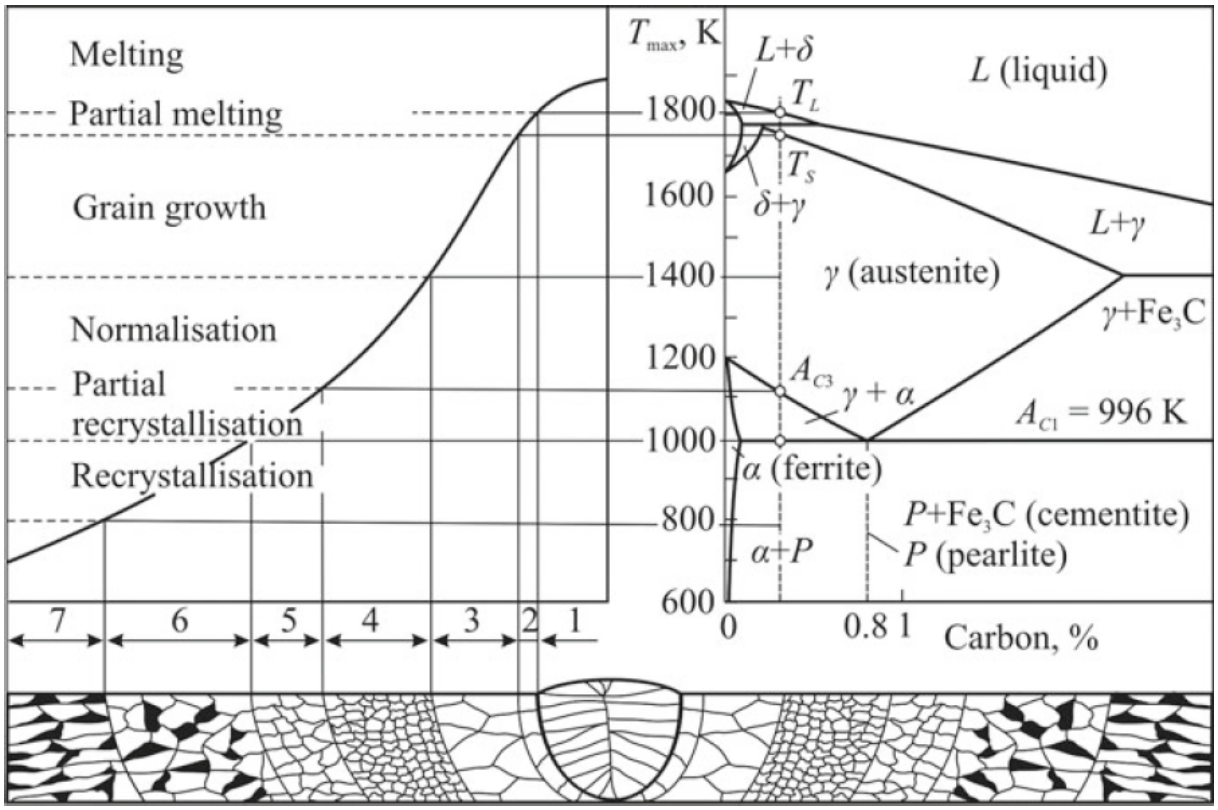

Figure 1.2: A section of a iron-carbide phase diagram with all the different zones that is appearing after a weld. This figure is taken from the book Karkhin [2013]

The different zones that are shown in figure 1.2 are:

1. The molten zone where all of the steel have been melted;
2. The partial molten zone here only some of the steel have been melted;
3. The grain growth zone where there will be severe grain growth since all the different carbides and nitrites have been dissolved;

4. The normalised zone where the all of the steel have been transformed into austenite, which then has been transformed to other phases;
5. Partial recrystallisation is the zone where only some of the steel has been transformed to austenite;
6. Recrystallisation is the zone where the internal energy is high enough so the grains can start to minimise the free surface energy by recrystallising the grains that have been plastically deformed, and finally
7. The unaffected zone which is the zone where nothing is happening.

The phases that austenite dissolves to are dependent on the cooling rate. For instance if the cooling time is low, it will mainly be formed into ferrite and pearlite. If it is a bit faster, bainite will also form, and if it is a lot faster, martensite will also form. The composition of these phases in the different heat affected zones are approximately the same, since it has been shown experimentally that the cooling rates for the different zone are nearly identical. [Karkhin, 2013].

2 | Simulation Set up

This simulation is built on the simulation and experimental work form the paper Sun et al. [2019]. Here, the setup is a plate with the dimensions of 300 mm × 200 mm × 8 mm that is subjected to a Tig-weld without filament. A sketch of the setup can be seen on figure 2.1. Further more there are two thermocouples in in the plate that are placed 1.8 mm and 3.5 mm from the fusion line. The grain structure is measured in the top by the use of x-ray diffraction in the coordinate x =0 mm y =150 mm, which is the red dot on figure 2.1b [Sun et al., 2019]. The weld data can be seen in table 2.1 [Sun et al., 2019]. The literature used in this part is livermore software technology corporation [2017a,b] unless otherwise mentioned. All keywords for this model can be found in appendix 5 on page 35

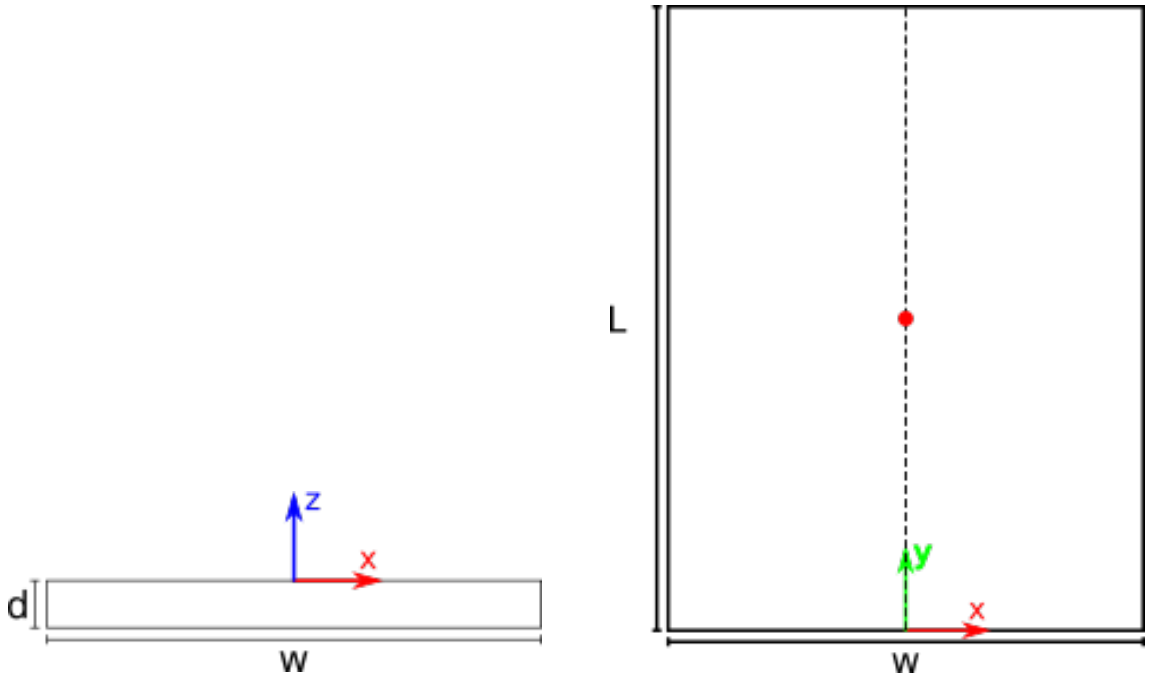

(a) Front view of the setup. The thickness is d and the width os w.

(b) Top view of the setup. The length is L, the width is w, and the dashed line is the weld line, the red dot is where the grain structure is measured.

Figure 2.1: The sketch of the model from different angles. The data for the model can be found in table 2.1 is provided by Sun et al. [2019].

Thickness (d) [mm]	Width (w) [mm]	Length (L) [mm]	Efficiency
8	200	300	0.50
Current [A]	Voltage[V]	Speed[$\frac{\text{mm}}{\text{s}}$]	Shielding gas
201	14.2	1.67	Ar

Table 2.1: Welding's input parameters from Sun et al. [2019], except for the efficiency which was not given. It has been found instead by trail and error.

It will be attempted to recreate their model using LS-Dyna, where the units used can be seen in

table 2.2.

Distance [mm]	Time [s]	Force [N]
Mass [ton]	Energy [mJ]	Stress [MPa]

Table 2.2: Units used for the simulations.

2.1 Mesh

The modelled plate is as mentioned a 300 mm × 200 mm × 8 mm ST355 steel plate, and this is meshed so the elements have the sizes of 1 mm × 1 mm × 1 mm, which can be seen on figure 2.2. The element used is a 8 node linear element with full integration for both temperature and displacements, which was chosen for its fast calculating time, then the quadratic elements. When reduced integration was attempted, the model turned out to be unstable, so full integration was necessary.

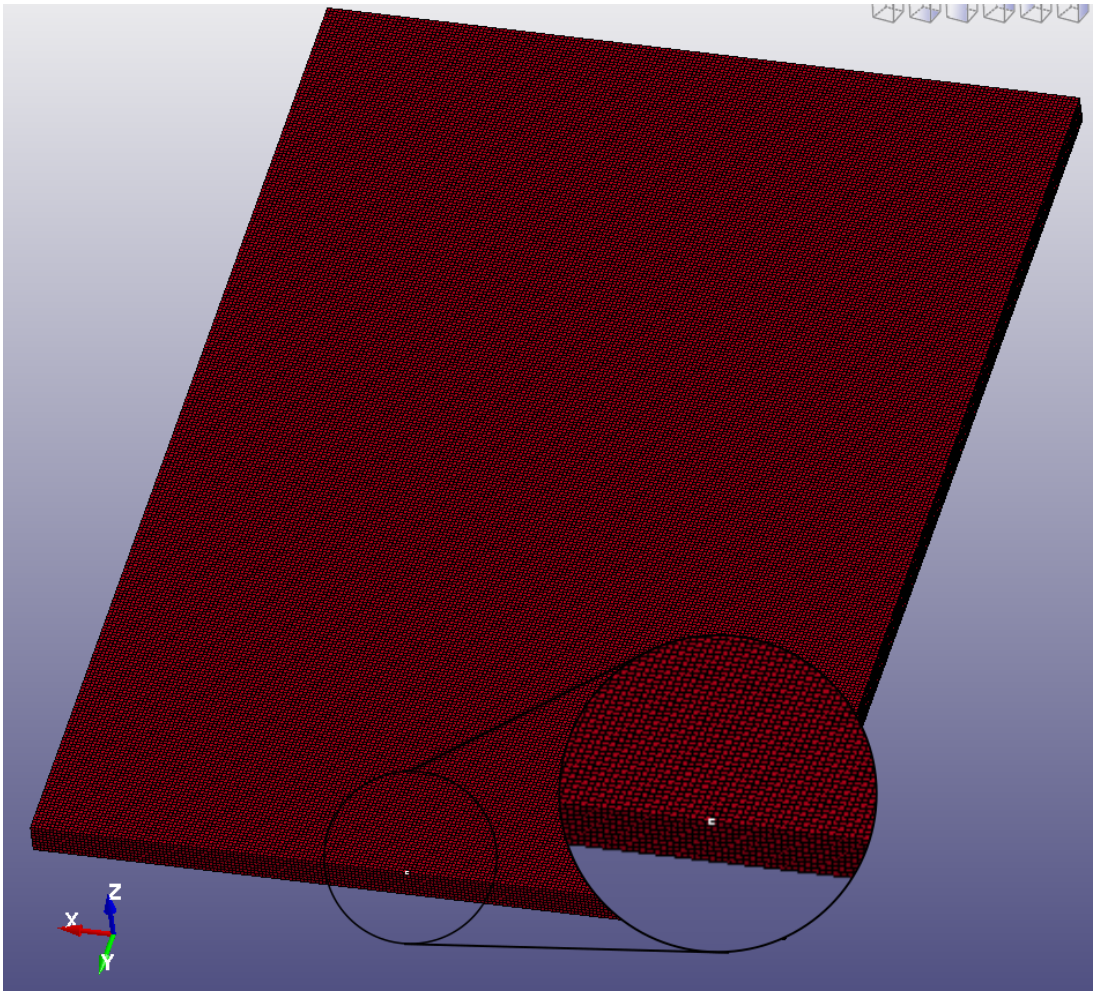

Figure 2.2: The mesh used for this simulation with the element size of 1 mm × 1 mm × 1 mm

These settings are implement by the the keywords showed under here, and the relevant entries will be explained.

```
*SECTION_SOLID
BlockMesh1
$#     pid     secid       mid     eosid      hgid      grav    adpopt      tmid
         1         1         2         0         0         0         0         2
$#   secid    elform       aet
         1         2         0
```

`pid` is a unique part id that will keep track of the different parts. `mid` is the unique id number for the material mechanical routine that is defined in section 2.4.1 on page 10. `tmid` is the unique id number for the thermal material routine that is defined in section 2.4.2 on page 14. Lastly, the `elform` is the element formulation which, when set to 2, is a 8 node linear formulation with full integration.

2.2 Heat input

To model the heat input, a Goldak-type of heat source is used, just as in the paper Sun et al. [2019]. Because they did not inform of any distribution parameters, these had to be found by trial and error. The same goes for the efficiency. The heat source is implement by the `*BOUNDARY_THERMAL_WELD_TRAJECTORY` as showed below.

```
*BOUNDARY_THERMAL_WELD_TRAJECTORY
$Weld line
$#     PID      PTYO     NSID1      VEL1      SID2      VEL2      NCYC   RELEVEL
         1         1         1       1.7        -3       0.0         4         0
$#   iform      lcid         Q     lcrot     lcmov     lclat      disc
         1         0   1407E3         0         0         0       2.0
$#      p1        p2        p3        p4        p5        p6        p7        p8
$ a radius   b Dept cf front  cr back Ff front        Fr         n
       4.1       4.1       3.5       6.0       1.3       0.7       4.0       0.0
```

`PTYO` is the number of parts in the weld, and `NSID1` is the list of elements that are the heat source is following. `VEL1` is the welding speed, which was given to be 1.7 $\frac{\text{mm}}{\text{s}}$, and `SID2` is a node set that the weld will be perpendicular to. `NCYC` is how many sub-divisions the heat energy will be divided over in a single time step. Setting it to 4 here makes it possible to have use slightly larger time steps. `iform` is where the heat distribution is chosen and 1 is the Goldak-type of destination, `Q` is the heat input, and since the efficiency was not given. Lastly, the inputs `p1` to `p8` are parameters to define the heat distribution. A sketch of how these parameters affect the weld can be seen on figure 2.3, and this figure is taken from the LS-Dyna manuals [livermore software technology corporation, 2017a].

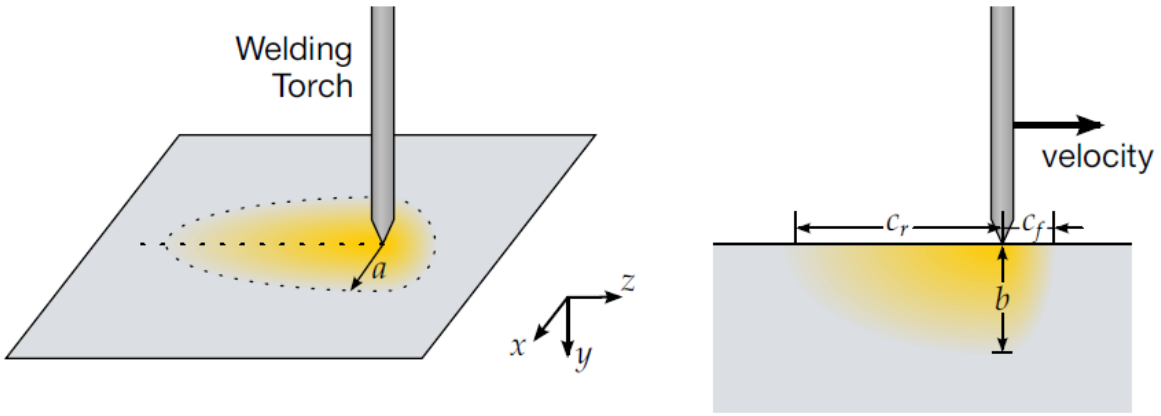

Figure 2.3: Sketch of how the input parameters for the heat distribution are related. This sketch is from livermore software technology corporation [2017a]

2.3 Solver

The whole analysis is set to simulate for 300 s. This is not enough time for the temperature to go back to room temperature, but it is well enough for the grain structure to form. The simulation time is implemented as showed below

```
*CONTROL_TERMINATION
$#  endtim    endcyc     dtmin    endeng    endmas
 300.00000
```

2.3.1 Themal Solver

The linear thermal solver is a symmetric direct solver which is implemented as shown below

```
*CONTROL_THERMAL_SOLVER
$     atyp     PTYPE    SOLVER     CGTOL       GPT    EQHEAT     FWORK       SBC
         1         2         1                   8
$   MSGLVL    MAXITR    ABSTOL    RELTOL     OMEGA                          STF
         0                                                                    1
```

where `atyp` is defining the type of thermal analysis. When set to 1 means it is a transient analysis, and `PTYPE` set to 2 means it is a non-linear problem with material properties calculated with the element mean temperature. `SOLVER` is set to 1 as default, which chooses a symmetric direct solver, where `GPT` defines how many gauss-points are used. When set to 8, it means that it solves using full integration.

The non-linear solver was set to a maximum of 40 matrix reformations per time step and the tolerance is set to 0.001. The implementation can be seen below.

```
*CONTROL_THERMAL_NONLINEAR
$#  refmax       tol       dcp    lumpbc    thlstl    nlthpr    phchpn
        40      1E-3  0.300000         1
```

`refmax` is where the number of max reformation is set, and `tol` is where the tolerance is set. `dcp` is a divergence control parameter where 0.3 was found sufficient, and `lumpbc` is a help function for radiation boundary condition.

2.3.2 Mechanical Solver

It was chosen to use an implicit solver since it allows for larger time steps. This is implemented by a multitude of keywords which will be explained here. First is `*CONTROL_IMPLICIT_GENERAL`:

```
*CONTROL_IMPLICIT_GENERAL
$#  imflag      dt0    imform     nsbs      igs     cnstn     form   zero_v
         1     0.01
```

Where `imflag` set to 1 enables the implicit analysis, and `dt0` is the first time step size. The next keyword is the `*CONTROL_IMPLICIT_AUTO`:

```
*CONTROL_IMPLICIT_AUTO
$#   iauto    iteopt    itewin    dtmin    dtmax    dtexp    kfail   kcycle
         2        11         5     0.01      4.0
```

Where `iauto` is set to 2 which allows for automatically adjusting the time step size, and `iteopt` is the optimal number of iterations in a time step. The time step size will not be changed as long as the number of iterations is in the interval `[iteopt-itewin,iteopt+itewin]`. `dtmin` is the minimum mechanical time step size and `dtmax` is the maximum step size. The maximal time step have been found not to effect the grain structure, since this measurement is made in the middle of the plate. Therefor there will be small time steps appropriately 90 s after, since the weld is going the hole length of the plate. The next keyword is the `*CONTROL_IMPLICIT_SOLUTION`:

```
*CONTROL_IMPLICIT_SOLUTION
$#  NSOLVR   ILIMIT   MAXREF    DCTOL    ECTOL    RCTOL    LSTOL   ABSTOL
        12                15     0.01     0.01
$    DNORM
         2
```

Where `NSOLVR` chooses the solver and the input 12 corresponds to a non-linear solver using the BFGS skim with the addition of the arc-length method. `MAXREF` is the number of reformations the stiffness matrix can make per time step. The tolerance is defined by `DCTOL` and `ECTOL`, where `DCTOL` is the displacement tolerance and `ECTOL` is the tolerance for the internal energy. Lastly `DNORM` gives the choice of how the displacement tolerance is defined. When set to 2, the tolerance is defined as increment over total displacement. The last keyword is `*CONTROL_IMPLICIT_SOLVER`:

```
*CONTROL_IMPLICIT_SOLVER
$#  LSOLVR   LPRINT    NEGEV    ORDER     DRCM   DRCPRM  AUTOSPC  AUTOTOL
         4        1                                 100        1    1.E-8
$#  LCPACK   MTXDMP
         2        0
```

Where `LSOLVR` chooses the linear solver. The default was chosen since it was deemed sufficient.

2.4 Material

The material input is divided in two: The Mechanical and the thermal material model. The mechanical material model is where the stresses and strains are calculated, while the thermal model calculates the temperature.

2.4.1 Mechanical Material model

The mechanical material model that have been used is `MAT_UHS_STEEL`. This material model has an implementation of the Kirkaldy model that is able to predict the grain structure during cooling. This model was first proposed by Kirkaldy and Sharma [1982] and is a phenomenological model based on the rate equation which can be seen in equation 2.1.

$$\frac{dF_i}{dt} = F_G F_C F_T F_f \tag{2.1}$$

Where :

F_G	$= 2^{\frac{G-1}{2}}$	is the contribution from the grain size;
F_C	$= \beta$	is the contribution from the composition of the steel;
F_T	$= (T_{cr} - T)^q e^{-\frac{Q_i}{RT}}$	is the contribution from the temperature, and
F_f	$= (f_a)^{\frac{2(1-f_a)}{3}} (1 - f_a)^{\frac{2f_a}{3}}$	is the contribution from the austenite left.

where G is the ASTM grain size, and β is a fitting parameter. T_{cr} is the critical formation temperature for a given phase, the Q_i is the activation energy for the phase. R is the gas constant, and f_a is the austenite fraction.

The input for this material model is explained here, and since there is a lot of input cards, they will be numbered:

```
*MAT_UHS_STEEL
$Card_1
$#     mid       ro        e       pr     tunit     crsh    phase     heat
        27.80000E-9  -111.0      0.3      0.0         0         0         2
```

`mid` is the material id, and `ro` is the density . `e` is where Young's modules are defined. Here it is defined as a function, and a graph of this which can be seen on figure 2.4, and it where obtained from Outinen and Mäkeläinen [2004] in lack of better sources. `pr` is Poisson's ratio, and `phase` is where the different phases can be toggled off. When set to 0, all phases are available. When `heat` is set to 2, the transformation to austenite during heating is active, and transformation from austenite during cooling. An explanation of how this transformation is calculated can be seen in appendix 5 on page 33.

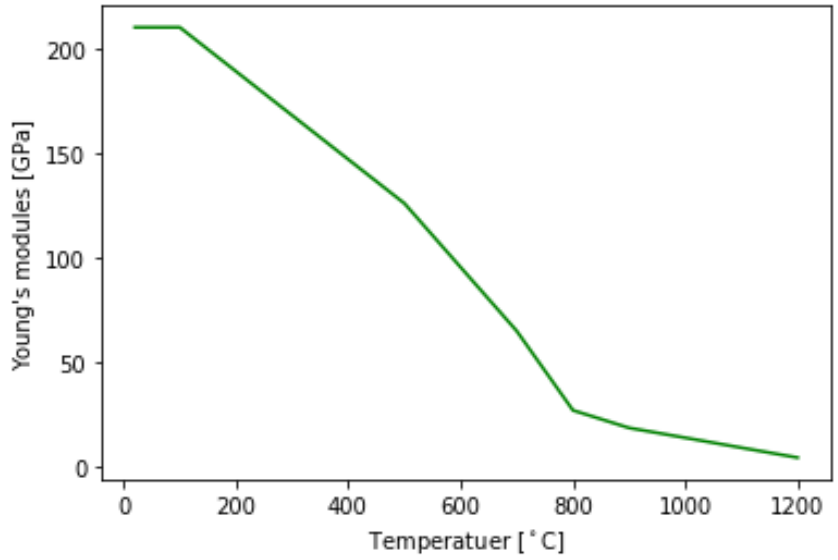

Figure 2.4: Young's modules as a function of temperature, obtained from Outinen and Mäkeläinen [2004]

```
$ Card_2
$#    lcy1     lcy2     lcy3     lcy4     lcy5     kfer     kper        B
      -666     -667     -667     -668     -669                      0.0
$ Card_3
$#       C       Co       Mo       Cr       Ni       Mn       Si        V
     0.067      0.0    0.004    0.015    0.012    1.270    0.008      0.0
$ Card_4
$#       W       Cu        P       Al       As       Ti      cwm    lctre
       0.0    0.018    0.009    0.049      0.0    0.001        1        0
```

The inputs `lcy1` to `lcy5` are the flow stress curves for the austinite, ferrite, pearlite, bainite and martensite respectively. These are temperature dependent and can be found in figure 2.5. The yield stress is read as the first entry in the data [Sun et al., 2019]. The parameters from `B` to `Ti` are the element contents in weight%. `cwm` set to one means that this material model is used for a welding analysis.

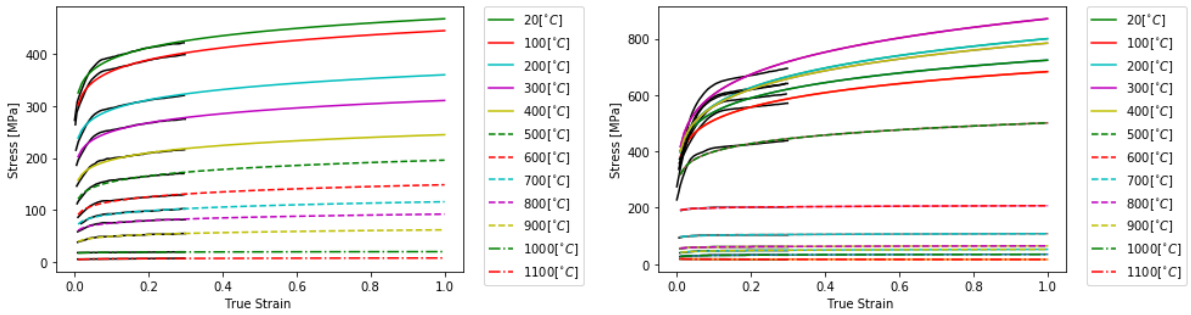

(a) Flow stress curves for austenite at different temperatures.

(b) Flow stress curves for ferrite and pearlite at different temperatures.

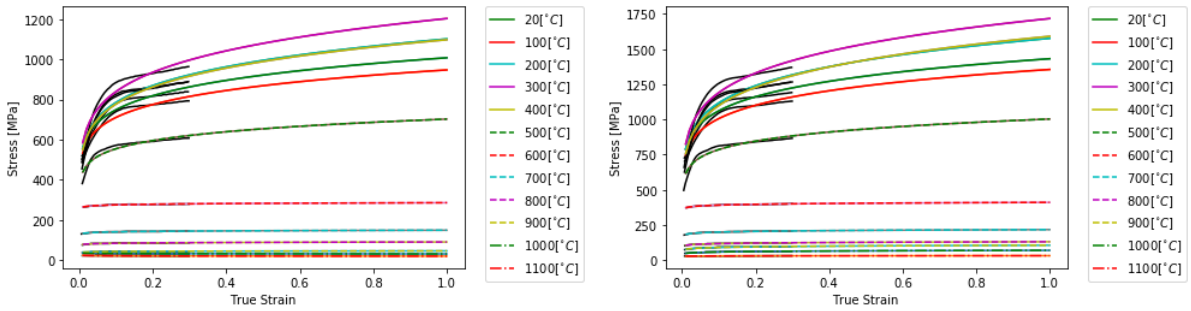

(c) Flow stress curves for bainite at different temperatures.

(d) Flow stress curves for martensite at different temperatures.

Figure 2.5: The different flow stress curves for both phases and temperature. The data is obtained from the paper Sun et al. [2019]

When examining the fitted curve and the data it can bee seen that the power law which is use dos not correspond well. Instead of using the power law $\sigma = K\varepsilon^n$, it could be beneficial to use a model that takes temperature into account such as the Johnson-Cook or Steinberg-Cochran-Guinan-Lund models [Banerjee, 2005]. But since obtaining the residual stress states is not the goal of this thesis, there were better ways to prioritise the time and effort it would have taken to make a better fit of the data.

```
$card_5
$#  thexp1    thexp5     lcth1     lcth5      tref      lat1      lat5     tabth
                          115        15    293.15   590E-3   640E-3         0
```

`lcth1` are the load curves for the thermal expansion coefficient for austenite and `lcth5`are for all the other phases. The data for this can be seen in figure 2.6 and is obtained from the paper Sun et al. [2019]. `lat1` and `lat5` are the latent heat energies for forming austenite to ferrite and martensite respectively.

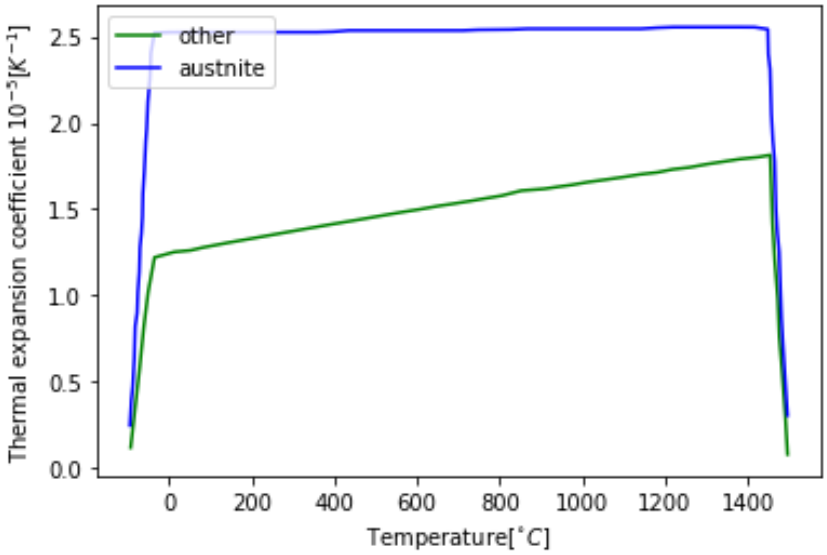

Figure 2.6: Thermal expansion as a function of temperature. This is obtained from the paper Sun et al. [2019].

```
$card_6
$#     qr2      qr3      qr4     alpha    grain    toffe    tofpe    tofba
    7743.0   10074.0  11301.0    0.011      8.7      0.0      0.0      0.0
```

Here `qr2`, `qr3`, and `qr4` are the Gibbs energies divided by the gas constant of the ferrite, pearlite, and bainite formation. `grain` is the ASTM grain size and since none was given in the paper Sun et al. [2019], a common value for low alloyed steel was chosen.

```
$card_8
$#    aust     ferr     pear     bain     mart      grk      grqr     tau1
       0.0     0.85     0.15      0.0      0.01.00000E12 30000.02.080000E8
$card_9
$#     gra      grb     expa     expb     grcc     grcm     heatn     tau2
       5.0   7375.0      1.0      1.0      1.0      1.0      1.0     4.806
```

`aust`, `ferr`, `pear`, `bain`, and `mart` are the start compositions of the steel. The last inputs are associated with grain growth and their values are the standard recommended values.

2.4.2 Thermal material

The Thermal material model that has been used are the `MAT_THERMAL_CWM`, and it is here the thermal material parameters are defined:

```
*MAT_THERMAL_CWM
$s355 solid
$#    tmid      tro    tgrlc   tgmult
         2      0.0      0.0      0.0
$#    lchc     lctc  tlstart    tlend  tistart    tiend   hghost   tghost
      2211     2212   -10000    -1000      0.0      0.0 650.000E6    0.001
```

`tmid` is the unique thermal material id number, and `lchc` is the specific heat capacity as a function of temperature. The data from this can be seen in figure 2.7b, and are obtained from Sun et al. [2019]. `lctc` is the load curve for the thermal conductivity, and the data can bee seen in figure 2.7a, and are obtained from Sun et al. [2019].

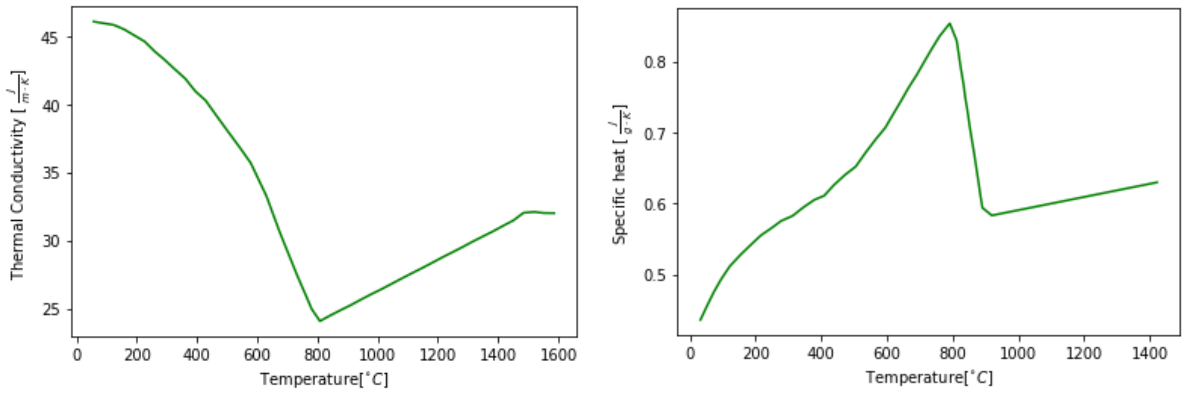

(a) Thermal conductivity as a function of temperature.

(b) Specific heat capacity as a function of temperature.

Figure 2.7: Thermal data for the model, obtained from the paper Sun et al. [2019].

2.5 Boundary conditions

The applied boundary conditions for this analysis will be mentioned here. The mechanical boundary conditions are chosen such that the plate is as simply supported as possible. One corner is restricted from moving in all directions, and the two adjacent corners have restrictions such that the plate can not rotating. A sketch of this can be seen on figure 2.8.

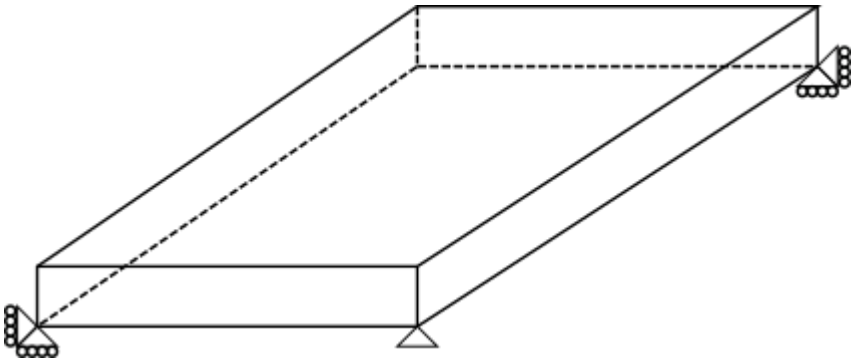

Figure 2.8: A sketch of how the boundary conditions are prescribed.

2.5.1 Thermal boundary

There are 3 thermal boundary conditions that are implemented. The first is a convection boundary between the steel plate and a steel welding table that is assumed to have an infinite mass. This boundary is applied at the xy plane where $z = -8\,\text{mm}$, the codinatesystem can be found on figure 2.1. The convection coefficient for this boundary was given to be $20\,\frac{\text{J}}{\text{m}^2\,\text{K}}$ [Sun et al., 2019]. The next boundary conditions is a radiation boundary. This boundary is applied to all other faces then the plate to welding table face. The emission coefficient (ε) of this boundary is set to 0.6 as given in Sun et al. [2019]. The last is the convection between air and the steel plate. Since the paper Sun et al. [2019] makes no mention of its value, this boundary have been obtained from literature [Jeberg, 2005; Karkhin, 2013], and the convection coefficient where here recommended to be $0.020\,\frac{\text{J}}{\text{m}^2\,\text{K}}$.

3 | Results

The results from the paper Sun et al. [2019] will be described here, and they will then be compared to the different analyses.

In the paper, they have measured the temperature in two points with thermocouples. The first was placed at 1.8 mm, and the second is 3.45 mm from the the border of the fusion zone Sun et al. [2019]. This is not very informative in itself, but it can be esteemed when comparing picture of the weld, and the temperatures from their FEM analysis. This can be seen on figure 3.1 which is obtained from the paper Sun et al. [2019]. Now it can be estimated where the two thermocouples are placed. Since there is a scale bar in figure 3.1, the first thermocouple (TC-1) is placed approximately 7 mm from the centre weld-line, and the second (TC-2) is approximately 8.5 mm form the weld-line centre.

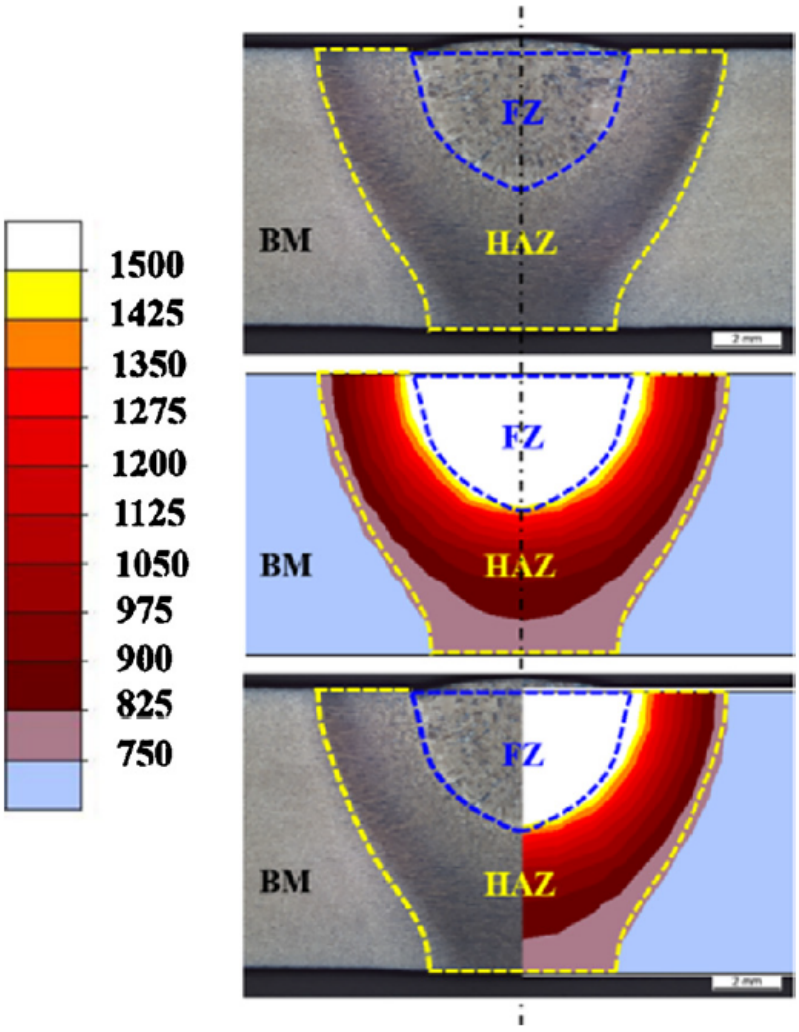

Figure 3.1: Resulting peak temperature found in the analysis done by Sun et al. [2019]. The scale bar in the bottom left corner is 2 mm

The measurement from these thermocouples can be seen in figure 3.2, which is obtained from the paper Sun et al. [2019]. Here the results from the simulation don by Sun et al. [2019] can also be seen, along site the cooling time from 800 °C to 500 °C.

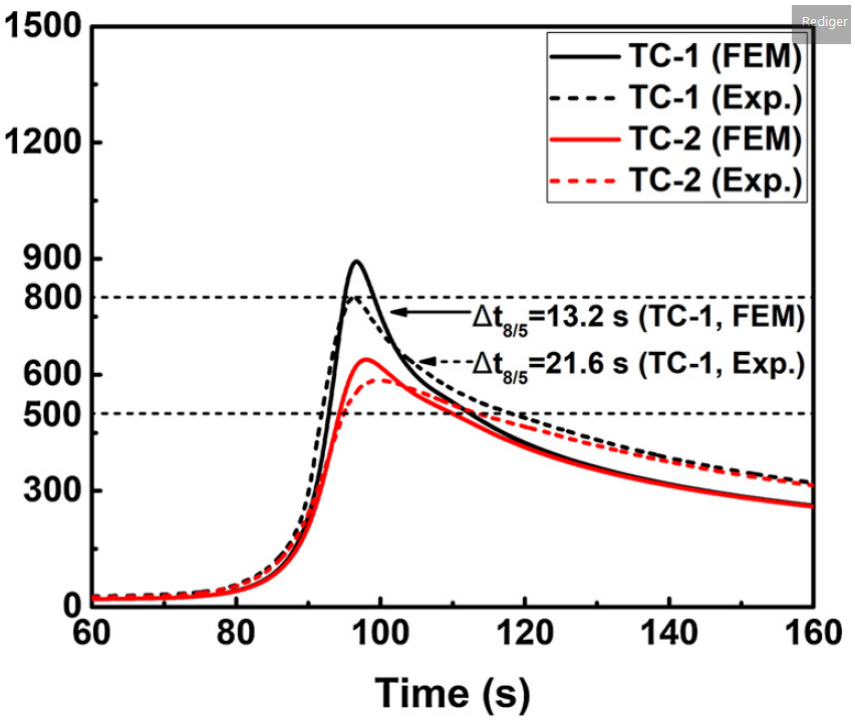

Figure 3.2: Temperature measured by the two thermocouples that are approximately placed 7 mm and 8.5 mm from the centre line. And the simulated temperature at this points, the cooling time from 800 °C to 500 °C is also given form both simulation and the experiment.

The cooling time and the resulting grain structures can bee found in table 3.1 [Sun et al., 2019].

	Coolingtime [s]	Ferrite-pearlite [wt%]	Bainite [wt%]	Martensite[wt%]
FEM	13.2	42	58	0
Measured	21.6	51	49	0

Table 3.1: The given grain structure from the centre of the weld-line, from both the simulation and meassurements done by Sun et al. [2019]

There is some disagreement between the experimental data and the simulation done by Sun et al. [2019]. It is clear that they either have too strict of an efficiency factor, or too efficient heat loss in their boundary.

3.1 Simulation results

Here the simulations that is explained in chapter 2 is used. The goal here is to recreate the temperature curves from the figure 3.2 as closely as possible. The resulting graphs can be seen in the figure 3.5. There has also been made a cut plot to see the comparison with the figure 3.1,

seen on figure 3.3. Comparing the size of the heat affected zones (HAZ) on the figure 3.3 with the size of the HAZ shown on figure 3.1, it is clear that the size of HAZ in this simulation is a bit smaller. This is probably because there is a lower amount of heat energy. This can mean either that the heat input is to low or that the heat is disappearing to fast.

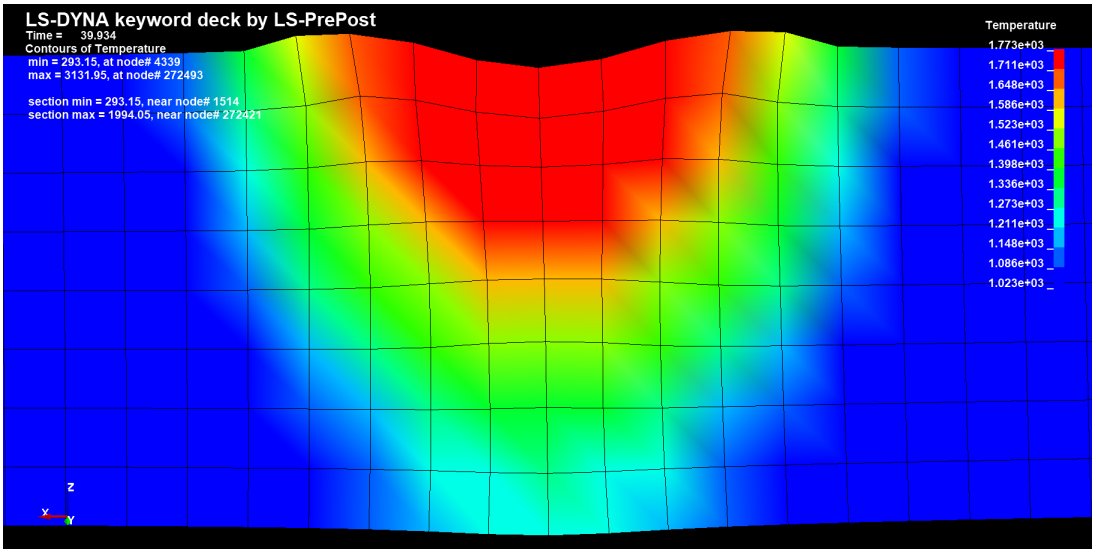

Figure 3.3: The temperature field in the first weld analysis. The cut made in the xz plane at $y = 150$ the coordinate system, is shown on figure 2.1. The starting mesh size is $1\,\text{mm} \times 1\,\text{mm} \times 1\,\text{mm}$ and the temperature is in Kelvin K.

The temperature is measured in 4 nodes, this 4 nodes are located as shown on figure 3.4, the white line is the xz-plane at $y = 150\,\text{mm}$. It can also be noted that the is some distorted that in cut can bee seen as in figure 3.11. This nodes have the x-coordinate of 6 mm, 7 mm, 8 mm and 9 mm, and when an intermediate point is needed the value is found by linear interpolation, as it is linear element that have been used. This appears as lines that is shown but is not a part of the grid mesh.

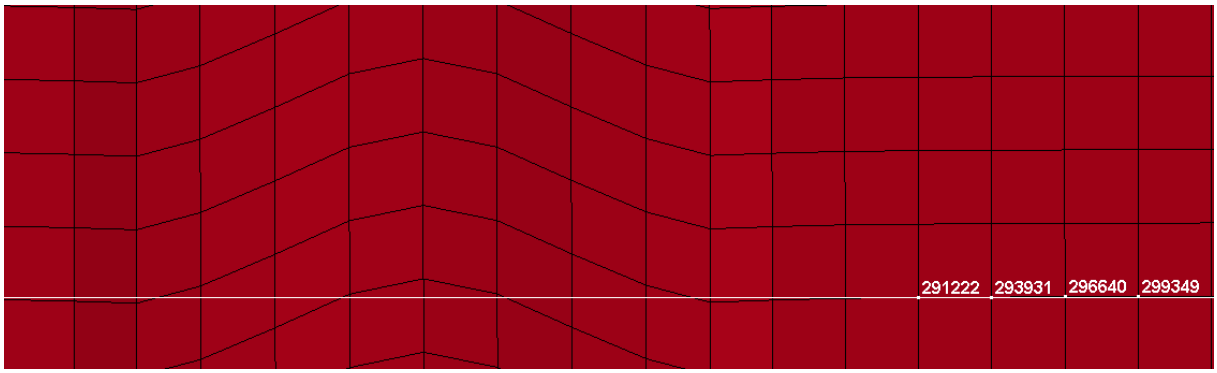

Figure 3.4: The yellow dots is the four notes where the temperature is measured, and the white line is the xz plane at $y = 150\,\text{mm}$.

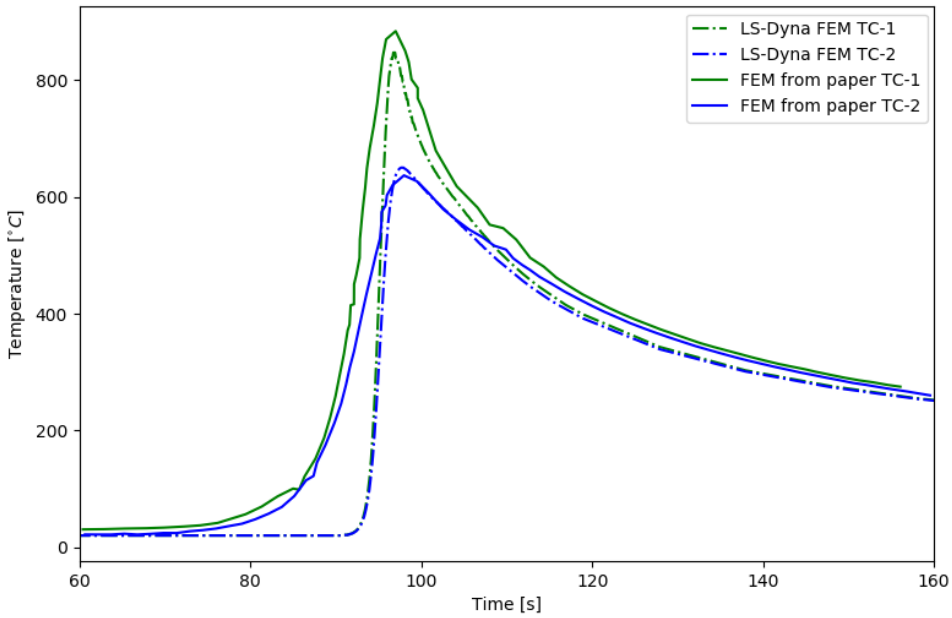

Figure 3.5: The simulated temperature from LS-Dyna here TC-1 and TC-2 are placed at 6.7 mm and 8 mm and the FEM analysis from Sun et al. [2019].

There are some differences to be seen here. The first is that the heating seems slower in the simulation done by Sun et al. [2019], but that is not of too large a concern because it is not a dominate feature for the determination of the grain structure. The main contributions are coming from the peak temperature and the cooling time between the temperature of 800 °C to 500 °C. Here, the simulations are in close agreement. The difference in peak temperature and in cooling time can be seen in table 3.2.

	Peak Temperature (TC-1)[°C]	Peak Temperature (TC-2) [°C]	Coolingtime [s]	Ferrite-pearlite [wt%]	Bainite [wt%]	Martensite [wt%]
FEM form the paper	883.8	636.7	13.2	42	58	0
LS-dyna	847.0	650.0	11.3	26	68	6

Table 3.2: Results from the FEM analysis and the results from Sun et al. [2019]'s FEM analysis.

3.2 Rosenthal

The Rosenthal solution is a theoretical model that is built on the following assumptions: The first and most important is that the welding process is quasi-stationary, so the coordinate system can follow the weld-pool. The second is that the weld is made on a semi-infinite plate. Lastly, it is assumed that there is no major loss of heat to the surroundings. This leads to the partial differential equation 3.1 [Nunes, 1983; Karkhin, 2013]:

$$\nabla^2 T + \frac{c\rho}{\lambda} v \frac{\partial T}{\partial x} = 0 \tag{3.1}$$

where:

∇	$= \left[\frac{\partial}{\partial x} + \frac{\partial}{\partial y} + \frac{\partial}{\partial z}\right]$	Nabla operater
c	$= 658\,\frac{\mathrm{J}}{\mathrm{kg\,K}}$	specific heat capacity
λ	$= 30\,\frac{\mathrm{J}}{\mathrm{m\,K}}$	thermal conductivity
ρ	$= 7874\,\frac{\mathrm{kg}}{\mathrm{m}^3}$	density
v	$= 1.67\,\mathrm{mm}$	welding speed

Both the specific heat capacity and the thermal conductivity are the average values from the input data on the figures 2.7 on page 14. This PDE has two solutions different solutions depending on the thickness of the plate. First there is a thin plate solution and second a thick plate solution. The difference for these two solution are that in the thin plate solution, the heat affected zone is going through the whole thickness, where in the thick plate solution, the heat affected zone does not. Therefore the heat in the thick- and thin plate solution will diffuse differently as shown on figure 3.6.

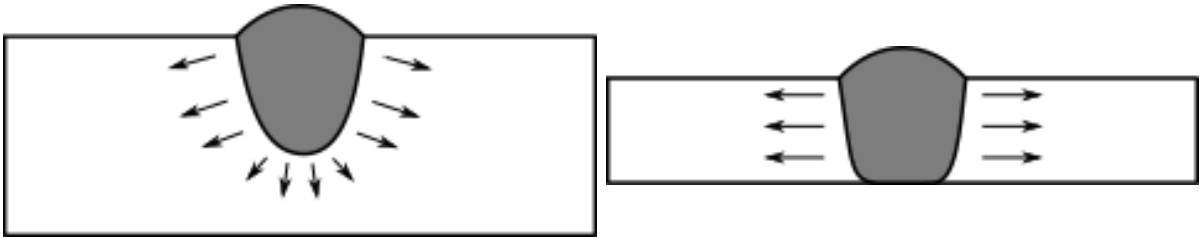

(a) Flux form the Thick plate solution.

(b) Flux form the Thin plate solution.

Figure 3.6: The flux from the two different solutions. The grey area is the heat affected zone.

To find which solution fits this problem, equation 3.2 is normally used [Nunes, 1983; Poorhaydari et al., 2005]. This equation calculates the critical thickness(d_c) where a switch in solution method is recommended [Nunes, 1983; Poorhaydari et al., 2005].

$$d_C = \sqrt{\frac{Q}{2\rho c} \cdot \left(\frac{1}{(500 - T_0)^2} - \frac{1}{(800 - T_0)^2}\right)} = 18.2\,\mathrm{mm} \tag{3.2}$$

Where T_0 is room temperature and Q is the Nominal heat input of $1.03\,\frac{\mathrm{kJ}}{\mathrm{mm}}$, and since the plate thickness $d_C > 8\,\mathrm{mm}$, the thin plat solution has been chosen. The solution of the PDE can be seen in equation 3.3 [Nunes, 1983; Poorhaydari et al., 2005].

$$T = T_0 + \frac{Q}{d\sqrt{4\pi\lambda\rho ct}} e^{\frac{-x^2}{4at}} \tag{3.3}$$

where x is the distance to the weld and a is the thermal diffusivity which is calculated as $a = \frac{\lambda}{\rho c}$. Lastly, when this equation is solved, and it yields the two curves that can be seen on figure 3.7.

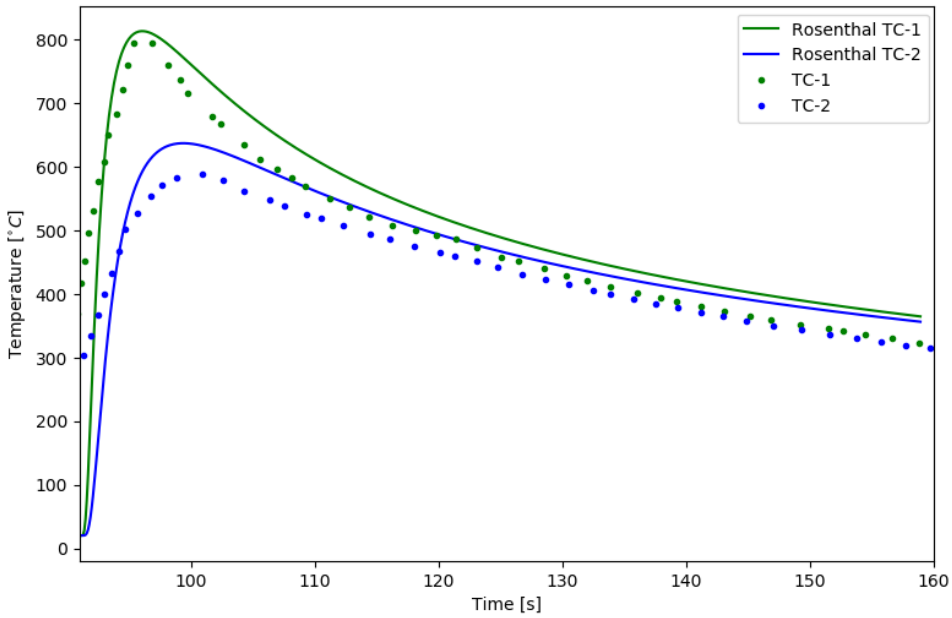

Figure 3.7: The solution of the Rosenthal equations in both TC-1 and TC-2 at 6.7 mm and 8 mm as well as the measurements done by Sun et al. [2019].

The Rosenthal equation does not work during the heating, but it will yield very good results for the peak temperature and the cooling sequence. It can be seen that the model over predicts the temperature. It also has a slower cooling time, which is 27.2 s while the data shows a cooling time of 21.6 s. It was tried to make an implementation of the Kirkaldy model for the Rosenthal solution which was unfortunately not successful. Therefor there is no estimation of the grain structure on the bases of the Rosenthal solution.

3.3 Comparison

When comparing the results, it is clear that there is a little difference between the FEM analysis from the paper Sun et al. [2019] and the the FEM and analysis made in this report. This small difference in the two FEM analyses has a large effect on the grain structure. Furthermore, it can be seen that there is some disagreement between the FEM analyses and the data. A plot of all these curves can be seen on figure 3.8.

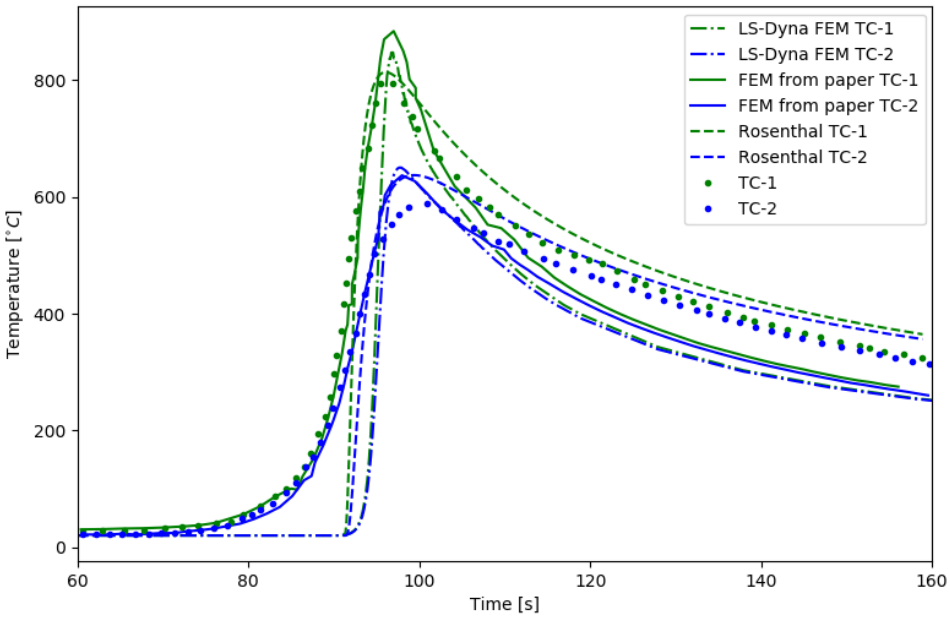

Figure 3.8: Results from figure 3.5 with the experimental data form Sun et al. [2019] added.

By looking at the figure 3.8, it is clear that the problem is most probably caused by the boundary condition between the steel table and the steel plate, which is drawing to much heat from the weld. Therefore a new analysis will be made with the convection coefficient of 5 mm.

When comparing the Rosenthal equation to the data from Sun et al. [2019], it can be seen that there is only a small disagreement, since the Rosenthal is overpredicting the temperature a little bit. This disagreement is probably due to the the assumption of no heat transport to the surroundings.

3.4 Improvements

As can be seen on figure 3.8, there is some disagreement between the finite element analyses and the measurements. This could be caused by the convection boundary being set to remove too much energy, therefor a analysis is made where the convection is lowered from 20 $\frac{\mathrm{J}}{\mathrm{m}^2\,^\circ\mathrm{C}}$ to 5 $\frac{\mathrm{J}}{\mathrm{m}^2\,^\circ\mathrm{C}}$. This resulted in the curves that can be seen in figure 3.10. A cut of this temperature has been made and can be seen on figure 3.9, where it once again is clear that the HAZ is smaller than the HAZ from figure 3.1.

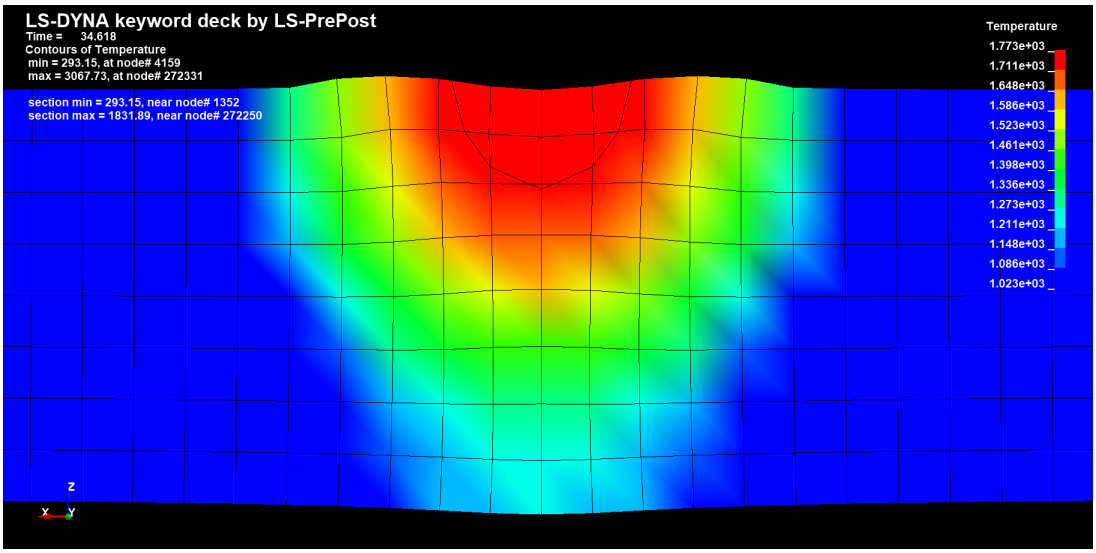

Figure 3.9: The temperature field in the second weld analysis. This cut is made in the xz plane at $y = 150$. The coordinate system is shown on figure 2.1, the starting mesh size is $1\,\text{mm} \times 1\,\text{mm} \times 1\,\text{mm}$, and the temperature is in Kelvin K.

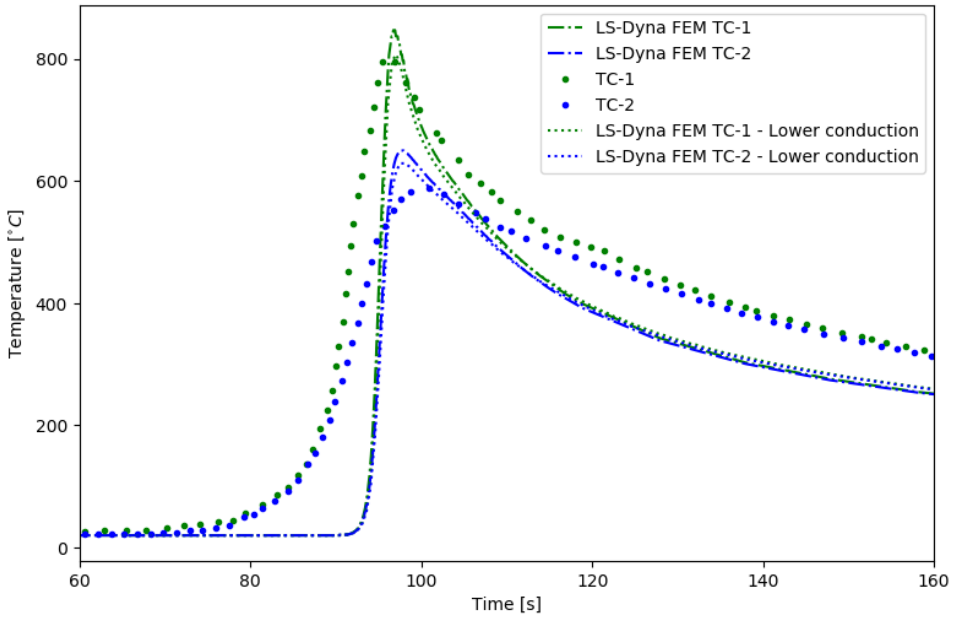

Figure 3.10: The effect of lowering the Convection boundary from 20 $\frac{\text{J}}{\text{m}^2\,^\circ\text{C}}$ to 5 $\frac{\text{J}}{\text{m}^2\,^\circ\text{C}}$, and here TC-1 and TC-2 are placed at 6.7 mm and 8 mm.

Here it can be seen that this makes nearly no difference and thus this can not explain the disagreement. Therefore the it must be the efficiency that has been increased to see if that can explain the difference. The result of this is shown in figure 3.12. There has also been made a cut of this temperature, which can be seen on figure 3.9. it can be seen here that the HAZ is a bit larger then the HAZ from figure 3.1.

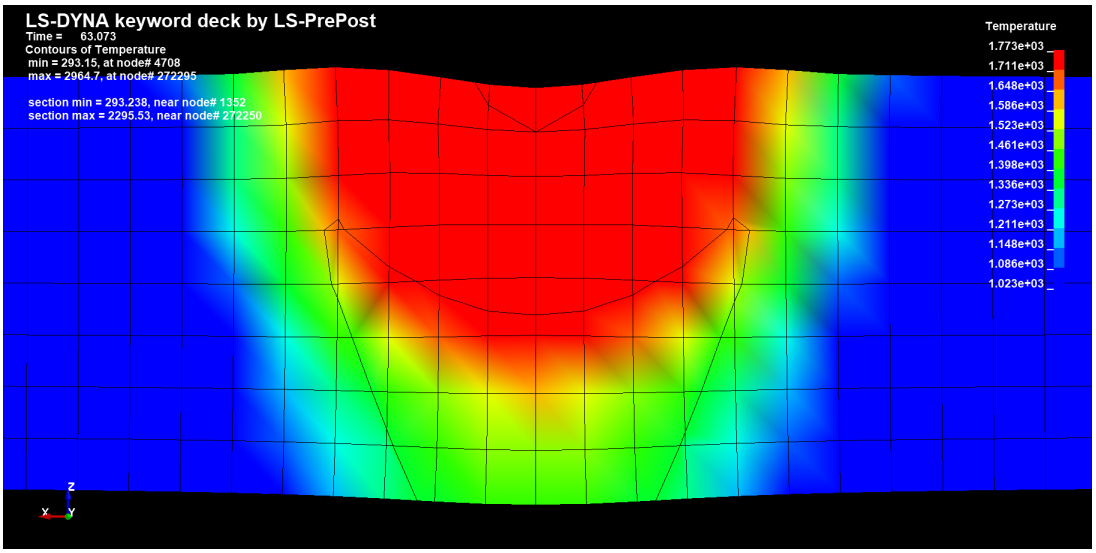

Figure 3.11: The temperature field in the third weld analysis. This cut is made in the xz plane at $y = 150$. The coordinate system is shown on figure 2.1, the starting mesh size is $1\,\text{mm} \times 1\,\text{mm} \times 1\,\text{mm}$, and the temperature is in Kelvin K.

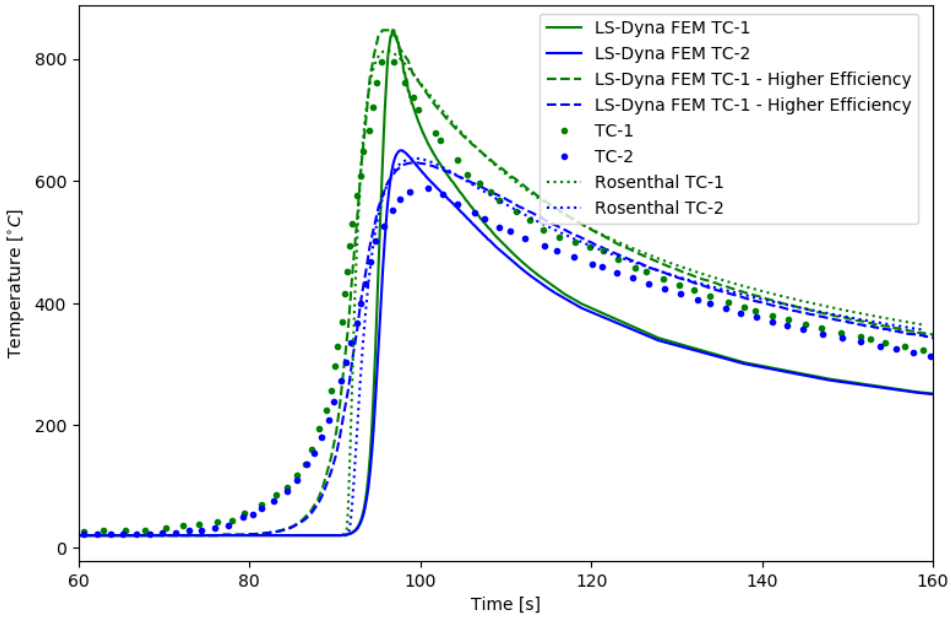

Figure 3.12: The effect of more energy input by increasing the efficency from 0.5 to 0.75, and here TC-1 and TC-2 are placed at 7 mm and 8.5 mm.

Here it can be seen that there is better agreement between the experiments an the simulation. It is important to notice that the measuring point has been moved slightly from 6.7 mm to 7 mm for TC-1 and 8 mm to 8.5 mm for TC-2. Since the stating placement of this are measured from a picture, it is therefore within a range that is deamed possible. For this analysis there is maybe a bit to much heat energy since the HAZ of the simulation is a bit larger then in figure 3.1. The resulting cooling rates and grain structure from these changes can be seen in table 3.3.

	Peak Temperature (TC-1)[°C]	Peak Temperature (TC-2) [°C]	Coolingtime [s]	Ferrite-pearlite [wt%]	Bainite [wt%]	Martensite [wt%]
FEM form the paper	883.8	636.7	13.2	42	58	0
LS-dyna	847.0	650.0	11.3	26	68	6
LS-dyna lower convection	807.0	618	12.1	54	45	1
LS-dyna higer efficiency	847.0	627.0	23.7	97	2	1
LS-dyna higer efficiency improved	847.0	627.0	23.7	56	44	0
Rosenthal	813.4	637.1	23.4	-	-	-
Measured	801.2	598.1	21.6	51	49	0

Table 3.3: The results of the improvements on the temperature.

There is not given any grain structure for the Rosenthal model, this is because a implementation of the Kirkarldy Model as shown in 2.4.1 have been troublesome and hard to get stable. Therefor it has not been possible to estimate the grain structure from this model. This is a shame since it is a closes fit to to the data.

Here it is clear that the more accurate temperature is producing a lot more ferrite and pearlite then was measured. This is probably due to the Gibbs energy being set to too low, in the material model, which has been tested to find a better fit. The Gibbs energy this resulted in is given as seen below.

```
$#     qr2       qr3       qr4     alpha     grain     toffe     tofpe     tofba
$     fer      pear      bain
    9617.9  12054.4  12054.4     0.011       8.7       0.0       0.0       0.0 $
```

The results of this can be seen in table 3.3 as LS-dyna higer efficiency improved. In the analysis with a lower convection, the grain structure is relatively close to the measured structure.

4 | Discussion

The data from Sun et al. [2019] makes it clear that there is some room for improvements, but that was not the first task. Since they did not provide all the essential information, certain factors such as the efficiency of the welding process had to be found. This was found to be 50% which is deemed quite low, since other sources such as Karkhin [2013]; Jeberg [2005]; Poorhaydari et al. [2005] show that the efficiency of a TIG weld should be around 75 % to 90 %. This is also much more in line with what is shown in the section 3.4 Improvements. Another constant that has not been mentioned is the convection constant between air and the steel plate. Some values were tested, but the effect was deemed negligible since it could bore no impact on the cooling time. Therefore the recommended value of 20 $\frac{\mathrm{mJ}}{\mathrm{m}^2\,\mathrm{K}}$ from Jeberg [2005]; Karkhin [2013] were used.

Another problem in recreating the results of the paper Sun et al. [2019] is deciding on the positions of the two thermocouples. These positions were given as distances from the border of the fusion zone. This information alone was not sufficient to locate the exact positions of these measurements. Therefore an approximate position was found by measuring on figure 3.1 on page 17, using the scale bar. This is location was found to be around 7 mm and 8.5 mm from the center of the weld line. All this leads to some problems since the two of the analyses "LS-Dyna" and "LS-Dyna with lower" convection have been measured to 6.7 mm and 8 mm, where LS-Dyna with higher efficiency have been measured 7 mm and 8.5 mm from the weld line center. This is a problem in the comparison form the different LS-Dyna analysis and the data form Sun et al. [2019]. Since a small change in the distance have a large effect on temperature profile.

Although there have been made some improvements on the cooling curves, it is clear that the resulting cooling time is greatly affecting the grain structure. This can especially be seen in table 3.3. Here the "LS-dyna" and the "LS-dyna with a lower convection" have a small difference in the cooling time of only 0.8 s. This results in a huge difference in the grain structure. This is an indication that the material model `MAT_UHS_STEEL`'s ability to predict the grain structure is rather unstable and requires that it is fitted to specific data. This was especially experienced when improving the grain structure results of "the LS-Dyna simulation with higher efficiency". Here the Gibbs energies was altered as shown in 3.4 to the values that are shown below.

```
$#     qr2       qr3       qr4     alpha     grain     toffe     tofpe     tofba
    9617.9   12054.4   12054.4     0.011       8.7       0.0       0.0       0.0 $
```

If this was altered to:

```
$#     qr2       qr3       qr4     alpha     grain     toffe     tofpe     tofba
    9620.0   12054.4   12054.4     0.011       8.7       0.0       0.0       0.0 $
```

The analysis would return 83% of martensite, 0% of bainite, and 17% ferrite-pearlite, and if changing the energies to:

```
$#     qr2       qr3       qr4     alpha     grain     toffe     tofpe     tofba
    9615.6   12054.4   12054.4     0.011       8.7       0.0       0.0       0.0 $
```

The results were 0% martensite, 3% bainite, and 97% ferrite-pearlite. Which lead to the understanding that there properly are some singularities in this model, and here one of them is most likely present.

5 | Conclusion

The differences in the simulation done by Sun et al. [2019] and the analysis done in LS-dyna are minor. This can be seen on figure 3.5 and it is also shown below in figure 5.1.

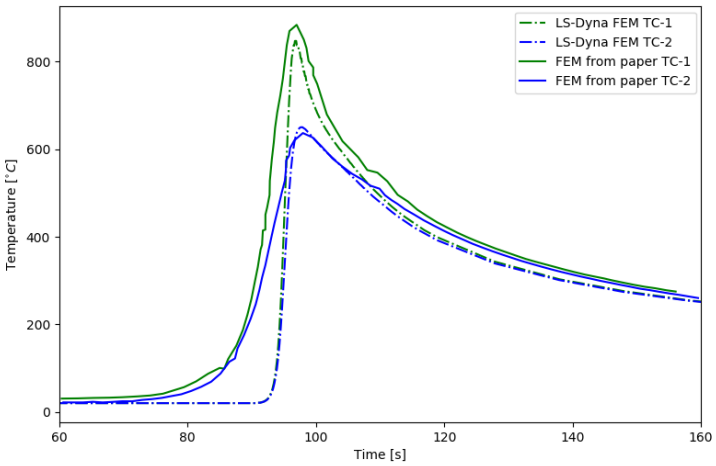

Figure 5.1: This is the same as 5.1, The simulated temperature from LS-Dyna and the FEM analsysis from Sun et al. [2019].

Here a small difference can noticed. The first is that the cooling time of the LS-Dyna analysis is 1.9 s lower than the analysis done by Sun et al. [2019], and there is a small difference in the predicted grain structure. The difference here was 10% for the bainite, 16% for the ferrite and pearlite, and lastly a 6% difference in martensite content.

The improvements that have been done show that Sun et al. [2019] probably have had too low of an efficiency, which was further supported by literature Jeberg [2005]; Karkhin [2013]. It was therefore not only possible to re-create their results but to improve them, with the best model having a difference in the cooling time by 2.1 s, where Sun et al. [2019] had 8.4 s. This improvement was also shown in the prediction of grain structure where the difference in ferrite pearlite was found to be 5% for the "LS-dyna higher efficiency improved" analysis, while Sun et al. [2019] had 9%. The difference in the prediction of bainite has the same tendency where the "LS-dyna higher efficiency improved analysis" shows a 5% difference, while Sun et al. [2019] has a 9% difference. Therefore it is deemed an overall better fit to the data than the model made by Sun et al. [2019].

Bibliography

Avrami, **1939**. Melvin Avrami. *Kinetics of phase change. I General theory.* The Journal of chemical physics, 7(12), 1103–1112.

Banerjee, **2005**. Biswajit Banerjee. *An evaluation of plastic flow stress models for the simulation of high-temperature and high-strain-rate deformation of metals.* arXiv preprint cond-mat/0512466.

Eisenhüttenleute, **1992**. Verein Deutscher Eisenhüttenleute. *Steel: a handbook for materials research and engineering.* vb. 1, Steel: A Handbook for Materials Research and Engineering. Springer. ISBN 9783540529682.

Fuchs and Stephens, **1980**. H.O. Fuchs and R.I. Stephens. *Metal fatigue in engineering.* Wiley-Interscience publication. Wiley. ISBN 9780471052647. URL `https://books.google.dk/books?id=mbxRAAAAMAAJ`.

Jeberg, **2005**. Peter Jeberg. *Automatic process optimised weld planning of full penetration I-joint GMA welding.* Denmark.

Kalpakjian et al., **2014**. Serope Kalpakjian, Stephen Schmid et al. *Manufacturing, Engineering and Technology SI 7th Edition-Serope Kalpakjian and Stephen Schmid: Manufacturing, Engineering and Technology.* Pea rson.

Karkhin, **2013**. Victor A Karkhin. *Thermal processes in welding.* St. Petersburg: St. Petersburg Polytechnical University.

Karlsson and Larsson, **1975**. B Karlsson and L-E Larsson. *Homogenization by two-phase diffusion.* Materials Science and Engineering, 20, 161–170.

Kirkaldy and Sharma, **1982**. J.S. Kirkaldy and R.C. Sharma. *A new phenomenology for steel it and CCT curves.* Scripta Metallurgica, 16(10), 1193 – 1198. ISSN 0036-9748. doi: https://doi.org/10.1016/0036-9748(82)90095-3. URL `http://www.sciencedirect.com/science/article/pii/0036974882900953`.

Koıstinen and Marbürger, **1959**. DP Koıstinen and RE Marbürger. *A General Equation Prescribing Extent of Austenite-Martensite Transformation in Pure Fe-C Alloy and Plain Carbon Steels.* Acta Metall, 7(1), 59–60.

livermore software technology corporation, **2017a**. livermore software technology corporation. *LS-DYNA® KEYWORD USER'S MANUAL VOLUME I.* livermore software technology corporation. manuals.

livermore software technology corporation, **2017b**. livermore software technology corporation. *LS-DYNA® KEYWORD USER'S MANUAL VOLUME II.* livermore software technology corporation. manuals.

Nunes, **1983**. AC Nunes. *An extended Rosenthal weld model.* Welding journal, 62(6), 165s–170s.

Oddy et al., **1996**. A. S. Oddy, J. M. J. Mcdill and L. Karlsson. *Microstructural Predictions Including Arbitrary Thermal Histories, Reaustenization and Carbon Segregation Effects.* Canadian Metallurgical Quarterly, 35(3), 275–283.

Outinen and Mäkeläinen, **2004**. Jyri Outinen and Pentti Mäkeläinen. *Mechanical properties of structural steel at elevated temperatures and after cooling down.* Fire and materials, 28(2-4), 237–251.

Poorhaydari et al., **2005**. K Poorhaydari, BM Patchett and DG Ivey. *Estimation of cooling rate in the welding of plates with intermediate thickness.* Welding journal, 84(10), 149s–155s.

Porter, **2018**. D.A. Porter. *Phase Transformations in Metals and Alloys.* Taylor & Francis Group. ISBN 9781138458079.

Saunders et al., **2004**. N Saunders, Z Guo, X Li, AP Miodownik and J Ph Schillé. *The calculation of TTT and CCT diagrams for general steels.* JMatPro Software Literature.

Speich et al., **1981**. GR Speich, VA Demarest and RL Miller. *Formation of austenite during intercritical annealing of dual-phase steels.* Metallurgical and materials transactions A, 12(8), 1419–1428.

Sun et al., **2019**. Jiamin Sun, Jonas Hensel, Jakob Klassen, Thomas Nitschke-Pagel and Klaus Dilger. *Solid-state phase transformation and strain hardening on the residual stresses in S355 steel weldments.* Journal of Materials Processing Technology, 265, 173–184.

Appendix A

The Formation austenite happens in three, the first is where the pearlite will transform to austenite This happens over the temperature of A_{c3}. There after ferrite well be in equilibrium with the austenite in the temperature range of A_{c3} to 912 °C. Then over the temperature 912 °C The ferrite will close to instantaneous transform to austenite [Oddy et al., 1996; Saunders et al., 2004; Karlsson and Larsson, 1975].

Pearlite to Austenite formation

The first formation is the model by the JMAK Model, since this proses dos not demand any diffusion there is no need for carbon diffusion [Avrami, 1939; Speich et al., 1981]. This formation will mainly start in the grain boundary, and there by the number of nucleation sites are constant. This can then be put in the JMAK Model, as can be seen in the equation 1 [Oddy et al., 1996; Speich et al., 1981].

$$f_\gamma(t) = 1 - e^{-t^3 \cdot (\frac{4\pi N}{3}) \cdot \dot{R}^3} \tag{1}$$

Where N is the number of nucleation sites, $\dot{R}$ is the formation rate. To Make these equation more useful in a finite element analysis this formulation needs to be a rate equation this can be don by first normalise to the equilibrium content as shown in equation 2 [Oddy et al., 1996; Speich et al., 1981]

$$F_a = f_a \cdot f_{eu}^{-1} = \left(1 - e^{-t^3 \cdot (\frac{4\pi N}{3}) \cdot \dot{R}^3}\right) \cdot \left(\frac{C_0 - C_\alpha}{C_{eu} - C_\alpha}\right)^{-1} \tag{2}$$

Then be differentiating the equation 2, and this yields the equation 3.

$$\dot{f_a} = 3 \left(ln\left(\frac{f_{au}}{f_{au} - f_a(t)}\right)\right)^{\frac{3-1}{3}} \left(\frac{f_{eu} - f_a(t)}{\tau}\right) \tag{3}$$

Formation of Austenite from Ferrite in the temperature range Ac_3 912 °C

The next formation process is the formation of austenite from ferrite, hear the carbon content is determined factor. Therefore The way to calculate the formation rate is by using the carbon

flux, the carbon transport is happening in two step, fist is from the Austenite formed from the pearlite to austenite with a varying carbon content. The next is the carbon flux from the the austenite and the ferrite. The Flux are calculated by Ficks fist law, and this can be seen in equation 4 [Oddy et al., 1996; Speich et al., 1981].

$$J_{12} = -(4\pi K_{12} D)\left(\frac{r_1^2 + r_2^2}{2}\right)\left(\frac{\bar{C}_{\gamma 2} - C_{eu}}{\frac{r_1+r_2}{2} - r_1}\right) \tag{4}$$

where K_{12} is correction factor that are 0.5, D is the diffusion coefficient r_1 and r_2 is the radius of the austenite formed by pearlite and the austenite with a varying carbon content respectively. $\bar{C}_{\gamma 2}$ is the average carbon concentration in the concentration varying zone, and C_{eu} is the carbon concentration in the austenite formed from pearlite.

There can now be made a rate equation that can be seen in equation 5 [Oddy et al., 1996; Speich et al., 1981]

$$\dot{f}_{\gamma 1} = \frac{-J_{12}}{(C_{eu} - \bar{C}_{\gamma 2})V} \tag{5}$$

where V is the total volume. this process can then be repeated for the for the next zone, and that rate equation can be seen in equation [Speich et al., 1981; Oddy et al., 1996].

$$\dot{f}_{\gamma 3} = \left(\frac{-3K_{23}D}{r_g^2}\right)\left(\frac{f_{\gamma 1}^{\frac{2}{3}} + (f_{\gamma 1} + f_{\gamma 2})^{\frac{2}{3}}}{(f_{\gamma 1} + f_{\gamma 2})^{\frac{1}{3}} - f_{\gamma 1}^{\frac{1}{3}}}\right)\left(\frac{\bar{C}_{\gamma 2} - C_{eq}}{\bar{C}_{\gamma 2} - C_{\alpha}}\right) \tag{6}$$

Appendix B

```
*CONTROL_CPU
$#  cputim
    0.000
$
*CONTROL_HOURGLASS
$#     ihq       qh
         6  0.100000
$
*CONTROL_SOLUTION
$#    soln      nlq     isnan     lcint
         2
$
$
*CONTROL_TERMINATION
$#  endtim    endcyc     dtmin    endeng    endmas
$       0.2
 300.00000
$
$
*CONTROL_TIMESTEP
$#  dtinit    tssfac      isdo    tslimt     dt2ms      lctm     erode     ms1st
           0.900000
$
$
*CONTROL_THERMAL_NONLINEAR
$#  refmax       tol       dcp    lumpbc    thlstl    nlthpr    phchpn
        40      1E-3  0.300000         1
$
$
*CONTROL_THERMAL_SOLVER
$     atyp     PTYPE    SOLVER     CGTOL       GPT    EQHEAT     FWORK       SBC
         1         2         1                   8     0.001
$   MSGLVL    MAXITR    ABSTOL    RELTOL     OMEGA                           STF
         0                                                                     1
*CONTROL_THERMAL_TIMESTEP
$#      ts       tip       its      tmin      tmax     dtemp      tscp      lcts
         1       1.0      0.01                4.0     250.0
$
*CONTROL_SOLID
$#   ESORT    FMATRX   NIPTETS   SWLOCL
         1         2
$
*CONTROL_IMPLICIT_GENERAL
$#  imflag       dt0    imform     nsbs       igs     cnstn      form    zero_v
         1      0.01                            1                             0
$
*CONTROL_IMPLICIT_AUTO
$#   iauto    iteopt    itewin     dtmin     dtmax     dtexp     kfail    kcycle
         2        11         5      0.01       4.0       0.0         0         0
$
*CONTROL_IMPLICIT_SOLUTION
$#  NSOLVR    ILIMIT    MAXREF     DCTOL     ECTOL     RCTOL     LSTOL    ABSTOL
        12                15      0.01      0.01
$    DNORM
         2
$
```

```
*CONTROL_IMPLICIT_SOLVER
$#  LSOLVR    LPRINT     NEGEV     ORDER      DRCM    DRCPRM   AUTOSPC   AUTOTOL
                 1                                      100         1     1.E-8
$#  LCPACK    MTXDMP
         2         0
$
$*DATABASE_BINARY_D3DUMP
$#      dt      lcdt      beam     npltc    psetid
$    0.005
$
*DATABASE_BINARY_D3PLOT
$#      dt      lcdt      beam     npltc    psetid
                620
$
*DEFINE_CURVE
$#      ID
       620
0 , 0.1
0.9, 0.1
1  , 0.5
159.5 , 0.5
160 , 10.0
1000 , 10.0
$
*DATABASE_EXTENT_BINARY
$    neiph     neips    maxint    strflg    sigflg    epsflg    rltflg    engflg
        23        23         3       111         1         1         1         1
$   cmpflg    ieverp    beamip     dcomp      shge     stssz    n3thdt   ialemat
         1         0         0         1         2         1
$  nintsld   pkp_sen      sclp    unused     msscl     therm    iniout    iniout
         1         0       1.0         0         2         2       ALL STRESS_GL
$
$Weld line
$#     PID      PTYO     NSID1      VEL1      SID2      VEL2      NCYC   RELEVEL
         1         1         1       1.7        -3       0.0         4         0
$#   iform      lcid         Q     lcrot     lcmov     lclat      disc
$         1         0    1519E3         0         0         0       2.0
         1         0    1970E3         0         0         0       2.0
$         1         0    2016E3         0         0         0       2.0
$         1         0    2268E3         0         0         0       2.0
$         1         0    2568E3         0         0         0       2.0
$         1         0    2800E3         0         0         0       2.0
$#      p1        p2        p3        p4        p5        p6        p7        p8
$ a radius   b Dept cf front  cr back Ff front       Fr         n
       4.1       4.1       3.5       6.0       1.3       0.7       4.0       0.0
$
*BOUNDARY_FLUX_SET
$#   secid
         2
$     LCID       MN1       MN2       MN3       MN4       LOC     NHIST
        -3        1.        1.        1.        1.
*DEFINE_CURVE
         3
-200000000.0 , 0
293.15 , 0
293.16 , 20E-3
1000000000 , 20E-3
$
$
*MAT_UHS_STEEL
```

```
$#     mid       ro        e       pr     tunit     crsh     phase     heat
         2 7.8000E-9   -111.0      0.3       0.0        0         0        2
$#    lcy1      lcy2     lcy3     lcy4     lcy5     kfer     kper        b
      -666      -667     -667     -668     -669 190000.0   3100.0      0.0
$#       c        co       mo       cr       ni       mn       si        v
$      0.13       0.0     0.03     0.09     0.12     1.37     0.22    0.036
     0.067       0.0    0.004    0.015    0.012    1.270    0.008      0.0
$#       w        cu        p       al       as       ti      cwm    lctre
$       0.0     0.25    0.016    0.002      0.0    0.006        1        0
       0.0    0.018    0.009    0.049      0.0    0.001        1        0
$#  thexp1   thexp5    lcth1    lcth5     tref     lat1     lat5    tabth
$2.51000E-51.11000E-5   -115      -15   293.155.900000E8 6.4000E8       0
         0        0      115       15   293.15   590E-3   640E-3        0
$   25.1E-6  11.1E-6        0        0   293.15    590E6    640E6      115
$#     qr2      qr3      qr4    alpha    grain    toffe    tofpe    tofba
$    5162.0   6716.0   7534.0    0.011      8.7      0.0      0.0      0.0 $ 0,5
$    6710.0   8730.8   9794.2    0.011      8.7      0.0      0.0      0.0 $ 0,65
$    7226.8   9402.4  10547.6    0.011      8.7      0.0      0.0      0.0 $ 0,70
    7743.0  10074.0  11301.0    0.011      8.7      0.0      0.0      0.0 $ 0,75
$    8259.2  10745.6  12054.4    0.011      8.7      0.0      0.0      0.0 $ 0,80
$    8775.4  11417.2  12807.8    0.011      8.7      0.0      0.0      0.0 $ 0,85
$   10324.0  13432.0  15068.0    0.011      8.7      0.0      0.0      0.0 $
$#  plmem2   plmem3   plmem4   plmem5     strc     strp    react   temper
       0.0      0.0      0.0      0.0      0.0      0.0        0        0
$#    aust     ferr     pear     bain     mart      grk     grqr     tau1
       0.0     0.85     0.15      0.0      0.01.00000E12  30000.02.080000E8
$#     gra      grb     expa     expb     grcc     grcm    heatn     tau2
       5.0   7375.0      1.0      1.0      1.0      1.0      1.0    4.806
$#             FS       PS       Bs       Ms     MSIG   LCEPS23   LCEPS4   LCEPS5
$ 1.092E+03 9.874E+02 8.511E+02 4.500E+02
$# tastart    taend  tlstart    tlend   eghost   pghost   aghost
     750.0    760.0-1.00000E8 -1000000   100.01.00000E-4     0.0
*MAT_THERMAL_CWM
$s355 solid
$#    tmid      tro    tgrlc   tgmult
         2      0.0      0.0      0.0
$#    lchc     lctc   tlstart    tlend   tistart    tiend   hghost   tghost
      2211     2212    -10000    -1000      0.0      0.0 650.000E6   0.001
$
*BOUNDARY_CONVECTION_SET
$#    SSID
         1
$#   HLCID    HMULT    TLCID    TMULT      LOC
$ air 10-100 w/(m^2 K^2)
$         0    1.5E-2        0      293
         0   20.E-6         0      293
$#   HLCID    HMULT    TLCID    TMULT      LOC
$         0   100.E-3        0      293
$
$*BOUNDARY_RADIATION_SET
$#    SSID     TYPE
$         1        1
$#   FLCID    FMULT    TLCID    TMULT      LOC
$ ORG
$         0 2.268E-17        0      293
$         0 2.268E-15        0      293
$         0 2.268E-12        0      293
         0 5.670E-17        0       293
$         0 5.670E-11        0       293
$         0 5.670E-11        0        20
```

```
$
```